



High capacity nanostructured $\text{Li}_2\text{Fe}_x\text{SiO}_4/\text{C}$ with Fe hyperstoichiometry for Li-ion batteries

Haitao Zhou, Mari-Ann Einarsrud, Fride Vullum-Bruer*

Department of Materials Science and Engineering, Norwegian University of Science and Technology, Alfred Getz v. 2, 7491 Trondheim, Norway

HIGHLIGHTS

- PVA-assisted sol–gel method was used to prepare nanoporous $\text{Li}_2\text{FeSiO}_4/\text{C}$.
- Pore size distribution was controlled by the parameters of the gel ageing process.
- Samples with large amounts of mesopores and macropores can give higher capacity.
- The amount of secondary phases was controlled by adjusting the Fe stoichiometry.
- The highest capacity resulted from gel aged at 24 °C for 10 h with Fe excess 10 mol%.

ARTICLE INFO

Article history:

Received 4 June 2012

Received in revised form

1 February 2013

Accepted 3 February 2013

Available online 17 February 2013

Keywords:

Lithium orthosilicate

Sol–gel

Pore size distribution

Fe stoichiometry

Lithium ion battery

ABSTRACT

$\text{Li}_2\text{FeSiO}_4$ -based materials have attracted a great deal of interest as cathodes for lithium ion batteries for its excellent thermal stability and good cycling ability. Nanoporous $\text{Li}_2\text{FeSiO}_4/\text{C}$ composites with varying Fe stoichiometry were synthesized by a PVA-assisted sol–gel method. Different gel formation processes were used to control morphology and pore size distribution. The pore size distribution was controlled by adjusting the parameters of the gel ageing process, the carbon content and phase purity was controlled by adjusting the starch content, and the amount of secondary phases was controlled by adjusting the Fe stoichiometry. The electrochemical properties of the $\text{Li}_2\text{FeSiO}_4/\text{C}$ composite were assessed using coin cells at 24 °C, and the optimized material showed an initial discharge capacity of 163 mAh g^{−1} at a discharge rate of C/16 ($C = 160 \text{ mA g}^{-1}$) and a high capacity retention of 96% after 200 cycles at a discharge rate of 1 C.

© 2013 Elsevier B.V. All rights reserved.

1. Introduction

The Li-ion battery is currently the battery technology with the highest energy density, volumetric as well as gravimetric. Since the cathode materials play an important role in the determination of energy density, safety and life cycle of Li-ion batteries [1], research and development of cathode materials is important for the further improvement of these batteries.

Polyanion materials have attracted a great deal of interest as cathodes for Li-ion batteries. The silicate materials Li_2MSiO_4 ($M = \text{Fe, Mn, Co, Ni}$) will in principle allow reversible extraction of two lithium ions, thus it should deliver higher capacity (333 mAh g^{−1}) compared to commercial cathode materials. This material also fulfils the need for potentially lower costs, high

thermal stability through strong Si–O bonding, increased safety, and environmental friendliness, making the material attractive as cathode material [2]. Unfortunately, the $\text{Li}_2\text{FeSiO}_4$ cathode materials reported in literature have shown low rate capability, resulting from low electronic and ionic conductivities [3]. The strategy to enhance the charge transfer is therefore to incorporate a carbon coating [4] and prepare a material with a designed nanoporous structure [5]. Nanoporous $\text{Li}_2\text{FeSiO}_4/\text{C}$ composites have recently been synthesized by the sol–gel method and different chelating agents such as citric acid [6], sucrose [4,7], polyethylene-poly (ethylene glycol) [8], polyvinylalcohol (PVA) [9], tartaric acid [10], and ascorbic acid [11] have been used. Other factors affecting the electrochemical properties of $\text{Li}_2\text{FeSiO}_4/\text{C}$ composites have also been investigated, such as carbon coating [3], particle size [12], carbon content [10], doping [13], heat treatment temperature [14], and heat treatment times [12].

In particular, for nanoporous electrodes, the pore size distribution (PSD) has been considered one of the most important

* Corresponding author. Tel.: +47 735 93976; fax: +47 735 50203.

E-mail address: vullum@nt.ntnu.no (F. Vullum-Bruer).

parameters, due to the difficulty of wetting of nanoporous electrodes [15]. Also, the accessibility of molecules such as $\text{Li}(\text{EC})_2^+$ and $\text{Li}(\text{EC})_3^+$ in an electrolyte [16] strongly depends on the pore size of the electrode [17]. Mesopores (≥ 2 nm) that are around two to three times larger than that of the electrolyte molecules have been considered as the most suitable [18] and this kind of pore morphology largely depends on the gel formation parameters [19,20]. Especially, the PSD for silica materials are strongly dependant on the gel ageing process [21], and a coarsened and strengthened structure can be developed after proper ageing [22]. However, there is no report on the effects of PSD on the electrochemical properties in the nanoporous $\text{Li}_2\text{FeSiO}_4/\text{C}$ composite prepared by the sol–gel method.

Another parameter that has been found to affect the electrochemical properties of the nanoporous $\text{Li}_2\text{FeSiO}_4/\text{C}$ composite is the amount of secondary phases formed by altering the Fe stoichiometry. One of these secondary phases is Li_2SiO_3 [11], which is an insulator [23] and not electrochemically active in the Li-ion battery [24]. Other secondary phases, such as Fe_{1-x}O [7], Fe_2O_3 [11], $\text{Li}_2\text{Fe}_3\text{O}_4$ [10], or LiFeO_2 [25] are electrochemically active, and when coated with carbon, can show high electronic conductivity and high discharge capacity, but poor capacity retention during cycling [26–29]. Previous work [9] has shown that even when stoichiometric amounts of Li-, Fe-, and Si-precursors are used, small quantities of secondary phases occur in the final material. It seems that a certain amount of secondary phases can give enhanced electrochemical properties compared to the phase pure $\text{Li}_2\text{FeSiO}_4$, and it is therefore important to obtain an understanding of the relationship between secondary phases and the electrochemical properties of the nanoporous $\text{Li}_2\text{FeSiO}_4/\text{C}$ composite.

In this study, $\text{Li}_2\text{Fe}_x\text{SiO}_4/\text{C}$ ($x = 1, 1.05, 1.1$) composites with optimized pore size distribution and varying Fe stoichiometry have been synthesized using a PVA-assisted sol–gel method combined with carbothermal reduction. Here, different gel formation parameters were used to control the morphology and PSD. Excess Fe was intentionally introduced to investigate the effect on the amount of secondary phases and also the electrochemical performance. The electrochemical properties were assessed using coin cells.

2. Experimental

2.1. Synthesis

$\text{Li}_2\text{FeSiO}_4$ was synthesized by a wet chemical method previously described [9]. The lithium precursor solution (5 M) was prepared by dissolving 0.05 mol pre-dried $\text{Li}(\text{CH}_3\text{COO}) \cdot 2\text{H}_2\text{O}$ (Sigma–Aldrich, reagent grade) in 10 mL distilled water. The iron precursor solution (1 M) was prepared by dissolving $\text{Fe}(\text{NO}_3)_3 \cdot 9\text{H}_2\text{O}$ (0.025 mol) (Sigma–Aldrich, >98%) in 25 mL distilled water. The concentration of metal cations in the aqueous Fe-solution was determined by thermogravimetry. The silicon precursor solution was prepared by dissolving 0.025 mol tetraethyl orthosilicate (TEOS) (Aldrich, >99%) in 10 mL ethanol. Polyvinylalcohol (PVA) solution was prepared by dissolving 1 g PVA (Aldrich, Mowiol 10-98, Mw = 61,000) in 20 mL distilled water at 150 °C for 5 min.

The standardized Li and Fe precursor solutions were weighed and mixed, and ethanol (10 mL) was then added to the solution. The TEOS solution was then added under vigorous stirring to produce a transparent solution. Finally, the PVA solution was added and stirring was done at 60 °C for 1 h in a covered beaker to ensure complete complexing of the metal cations. The pH value of the solution was ~ 1 .

Gel formation took place after stirring the solution for 6 h at 60 °C in the uncovered beaker. Three gel formation methods were

used to prepare the materials. For the first method, the gel was directly dried at 130 °C for 3 h without ageing. For the second method, the gel was covered and aged at 24 °C for 10 h before drying at 130 °C for 3 h. For the third method, the gel was covered and aged at 60 °C for 10 h before drying at 130 °C for 3 h. All the Li–Fe–Si-containing dry gels were calcined at 450 °C for 1 h in air. The calcined powder was then mixed with an aqueous corn starch (Sigma–Aldrich, reagent grade) solution and ground into a paste in an agate mortar. The powder mixtures (starch content = 27 wt%) were heat treated in a flowing N_2 atmosphere at 650 °C for 10 h. These three $\text{Li}_2\text{FeSiO}_4/\text{C}$ samples were categorized to series 1.

In order to explore the effect of varying starch content on the phase composition, the 60 °C aged and calcined Li–Fe–Si powders were mixed with different amounts of starch (1, 10, 24, 27, 35, and 50 wt%), and heat treated in a flowing N_2 atmosphere at 650 °C for 10 h. These six $\text{Li}_2\text{FeSiO}_4/\text{C}$ samples were categorized to series 2.

In order to explore the effect of secondary phases on the electrochemical performance, 5 and 10 mol% Fe excess $\text{Li}_2\text{Fe}_x\text{SiO}_4/\text{C}$ ($x = 1.05, 1.1$) samples were also prepared by two different gel formation methods (24 °C or 60 °C ageing) with 27 wt% starch. These four $\text{Li}_2\text{FeSiO}_4/\text{C}$ samples were categorized to series 3. All the samples with different preparation methods are listed in Table 1.

2.2. Characterization

All the powders were analyzed by X-ray diffraction (XRD) using Cu K α radiation (Bruker AXS D8 FOCUS diffractometer with a LynxEye PSD). TOPAS R (Bruker AXS) version 2.1 was used for X-ray Rietveld refinements. The specific surface area and pore size distribution were analyzed by nitrogen adsorption measurements (Tristar 3000 Micrometrics). The carbon content of selected samples was tested by using a combustion-method (Molab AS). The morphology of the products was studied using field emission scanning electron microscopy (FESEM, Hitachi S-4300SE) and transmission electron microscopy (TEM, JEOL 2010F operated at 200 kV). TEM samples were prepared by dispersing the powders on a holey carbon-coated Cu TEM grid. Inter planar d -spacings were measured directly from the HRTEM image by measuring the distance between a selected number of lattice planes [30]. The magnification in the TEM images is calibrated to an accuracy of $\pm 2\%$. The elemental compositions of the particles were determined by an Oxford Instruments Energy Dispersive Spectrometer (EDS) attached to the TEM.

The electrochemical properties of the $\text{Li}_2\text{FeSiO}_4/\text{C}$ composite were assessed using CR2016 coin cells. The cathode was prepared by mixing 85 wt% of the $\text{Li}_2\text{FeSiO}_4/\text{C}$ composite with 10 wt% Supper-P carbon black and 5 wt% poly-vinylidene fluoride (PVDF) (Kynar, reagent grade). A slurry was made by ball milling, using N -methyl-2-pyrrolidone (NMP) (Sigma–Aldrich, >99%) as the solvent. The electrodes were formed by tape casting the slurry onto Al foil, followed by drying overnight at 90 °C in a vacuum furnace. A typical cathode loading was 4–5 mg cm^{-2} . Coin cells were assembled with the cathode, lithium metal as the anode and a Celgard 2400 film as the separator. The electrolyte used was 1 M LiPF_6 (Aldrich, >99.99%) dissolved in ethylene carbonate (EC, Sigma, 99%)/diethyl carbonate (DEC, Aldrich, >99%) (3:7 volume ratio). Cell assembly was carried out in an argon-filled glove box, where water and oxygen concentrations were 0.1 ppm. Charge–discharge analysis was performed galvanostatically between 1.5 and 4.2 V at 24 °C. All reported capacities are quoted with respect to the mass of the $\text{Li}_2\text{FeSiO}_4/\text{C}$ composite, including the carbon and the secondary phases.

Geometry optimization calculations of the electrolyte molecules $\text{Li}(\text{EC})_2^+$ and $\text{Li}(\text{EC})_3^+$ were conducted with the use of the GULP code [31], and the Universal force field [32] was considered.

Table 1
Li₂Fe_xSiO₄/C made with different preparation methods and carbon contents.

Series No.	Sample code ^d	Li ₂ Fe _x SiO ₄ /Fe stoichiometry	Gel ageing	Starch content (wt%)	Carbon content after 450 °C calcination	Carbon content after carbothermal reduction
1 ^a	NoaFe1St27	1	Non-aged	27	1.80	
	24aFe1St27	1	24 °C	27	1.47	
	60aFe1St27	1	60 °C	27	0.83 ^e	4.98
2 ^b	60aFe1St1	1	60 °C	1		
	60aFe1St10	1	60 °C	10	0.83 ^e	1.56
	60aFe1St20	1	60 °C	20	0.83 ^e	4.04
	60aFe1St24	1	60 °C	24	0.83 ^e	5.64
	60aFe1St35	1	60 °C	35	0.83 ^e	9.24
	60aFe1St50	1	60 °C	50	0.83 ^e	
3 ^c	24aFe1.05St27	1.05	24 °C	27		
	60aFe1.05St27	1.05	60 °C	27		
	24aFe1.1St27	1.1	24 °C	27		
	60aFe1.1St27	1.1	60 °C	27		

^a Ageing condition changed.

^b Starch content varied.

^c Fe stoichiometry varied.

^d Noa: Non-aged; 24a: 24 °C aged for 10 h; 60a: 60 °C aged for 10 h; Fe1: Li₂FeSiO₄; Fe1.05: Li₂Fe_{1.05}SiO₄; Fe1.1: Li₂Fe_{1.1}SiO₄ St27: 27 wt% starch content.

^e Prepared from the same batch.

3. Results

3.1. Phase analysis

3.1.1. Effects of the gel formation parameters on the phase composition

Fig. 1a shows the XRD patterns of Li₂FeSiO₄/C series 1 samples obtained using different PVA-assisted gel formation parameters with 27 wt% starch. The Li₂FeSiO₄ phase in the three samples could be identified by the space group $P2_1/n$ [33]. The additional diffraction lines appearing at approximately 37°, 43°, and 62° were ascribed to a α -LiFeO_{2-x} related phase [34], which was indexed in the cubic system (Fm-3m). A Li₂SiO₃ secondary phase with space group Cmc2₁ [24] could also be observed in Fig. 1.

The Rietveld refinement of sample NoaFe1St27 is shown in Fig. 1b. The calculated cell parameters of the Li₂FeSiO₄ phase are $a = 8.222(8)$ Å, $b = 5.009(5)$ Å, $c = 8.239(3)$ Å, and $\beta = 98.91(2)^\circ$. The calculated cell parameter of the α -LiFeO_{2-x} related phase is $a = 4.189(6)$ Å, which is slightly larger than the literature value of the α -LiFeO₂ phase ($a = 4.158$ Å, JCPDS17-938), and similar to the value of Li_{0.5}Fe_{0.5}O_{0.8} ($a = 4.197$ Å, JCPDS7-9428), which is cubic and isostructural with α -LiFeO₂. This increase in the lattice constant is expected as a part of the Fe³⁺ ions were reduced to larger Fe²⁺ ions (Fe³⁺ and Fe²⁺ ionic radii are 0.079 and 0.092 nm [35], respectively) during the carbothermal reduction. The Rietveld refinement results for all the samples are listed in Table S2. Sample 60aFe1St27 which was aged at 60 °C showed higher content of Li₂SiO₃ and α -LiFeO_{2-x} related phases compared to samples NoaFe1St27 and 24aFe1St27. This sample (60aFe1St27) turned non-transparent and expelled a small amount of liquid phase after ageing at 60 °C. The non-transparency was due to precipitation of LiNO₃, which was confirmed by XRD (Fig. S1). The measured carbon residue contents were 1.80, 1.47, and 0.83 wt% for samples NoaFe1St27, 24aFe1St27, and 60aFe1St27 before carbothermal reduction, respectively, as listed in Table 1.

3.1.2. Effects of starch content on the phase composition and carbon content

The XRD patterns of Li₂FeSiO₄/C series 2 samples are shown in Figure S2 and the XRD Rietveld refinements are listed in Table S1. The relationship between the phase composition and starch content is similar to our previous work [9]. However, the α -LiFeO_{2-x} related phase was considered in this work and a high yield of the Li₂FeSiO₄ phase was obtained with starch contents of 10–50 wt%. Fig. 2 shows the carbon content of Li₂FeSiO₄/C prepared by ageing

the gel at 60 °C and varying content of starch (10, 20, 24, 27 and 35 wt%). The amount of residual carbon increased almost linearly with increasing wt% of starch.

3.1.3. Effects of Fe excess on the phase composition

Fig. 3a shows the XRD patterns of the Li₂Fe_xSiO₄/C series 3 samples ($x = 1.05, 1.1$) obtained by ageing the gel at 24 °C and 60 °C, using 27 wt% starch. In addition to the major phase, Li₂SiO₃ and α -LiFeO_{2-x} related secondary phases were observed in all the four samples. XRD Rietveld refinements of the products are listed in Table S1. The relationships between the phase purity and Fe stoichiometry for the two different gel ageing temperatures are provided in Fig. 3b. Samples aged at 24 °C, all show ~90 wt% yield of Li₂FeSiO₄ and the content of the α -LiFeO_{2-x} related phase increases with increasing Fe excess. The Li₂SiO₃ phase shows the opposite trend. Sample 24aFe1.1St27 presented the highest yield of Li₂FeSiO₄ and α -LiFeO_{2-x} related phase, while the intensity of the diffraction lines for Li₂SiO₃ was very low, indicating a barely detectable amount of this phase. For samples aged at 60 °C, the yield of Li₂FeSiO₄ was lower than for the samples aged at 24 °C, and showed a maximum at $x = 1.05$, as provided in Fig. 3c.

3.2. Pore morphology

3.2.1. Effects of gel formation parameters on the pore morphology

The field emission scanning electron microscope (FE-SEM) images of the three Li₂FeSiO₄/C samples in series 1 obtained by different PVA-assisted gel formation processes are shown in Fig. 4(a–c). The samples are built up of nanoparticles, with a smooth surface and a typical diameter of 20–30 nm. The non-aged sample contained few meso-scale pores. The samples aged for 10 h at 24 and 60 °C, respectively, contained a large amount of pores with uniform pore morphology and distribution. Most of the pores are mesopores with pore sizes of ~20–30 nm. The pore structure analysis based on nitrogen adsorption measurements is given in Fig. 4(d–f). The BET surface areas of the three samples (Fig. 4d) show that the differences in the total surface area are relatively small. The differences in the pore size distribution however, are quite significant and for the non-aged sample nearly half of the total surface area (S_{BET}) was due to micropores (S_{mic}). After ageing at 24 °C, S_{mic} decreased by approximately 50% compared to sample NoaFe1St27, while the external surface area ($S_{\text{mes+mac}}$) increased accordingly, rendering the total surface area nearly unchanged. After ageing at 60 °C, there were no micropores observed and the total surface area (S_{BET}) was contributed by $S_{\text{mes+mac}}$. The increase

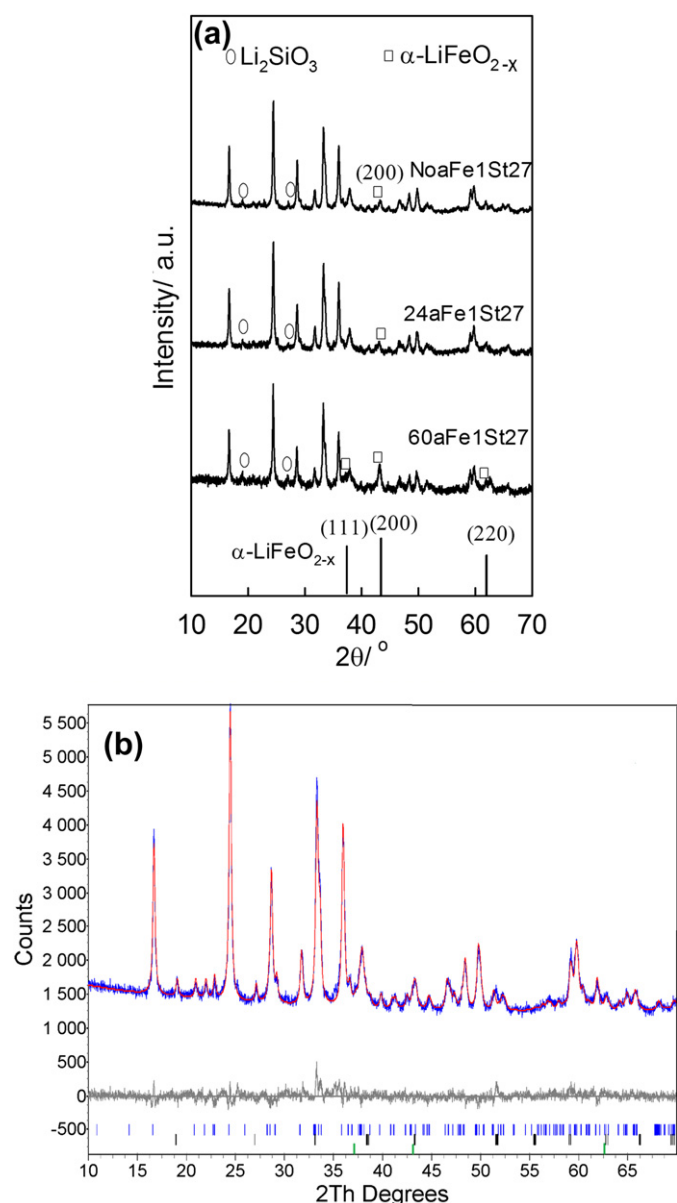


Fig. 1. (a) XRD patterns of $\text{Li}_2\text{FeSiO}_4/\text{C}$ series 1 samples obtained by different PVA-assisted gel formation processes with 27 wt% starch. (b) Experimental XRD data (blue line) of sample NoaFe1St27 with fitted pattern (red line), Bragg positions (blue markers for $\text{Li}_2\text{FeSiO}_4$, $\text{P}2_1/n$, black markers for Li_2SiO_3 , green markers for $\alpha\text{-LiFeO}_{2-x}$ related phase) and difference curve (grey line). (For interpretation of the references to colour in this figure legend, the reader is referred to the web version of this article.)

of $S_{\text{mes+mac}}$ coincided with the increase of the fraction of mesopore and macropore volume ($V_{\text{mes+mac}}$) of the total pore volume (V_{total}), as shown in Fig. 4e. Fig. 4f shows the PSD of the three samples. The mesopore volume increased dramatically for aged samples compared to the non-aged sample. The amount of mesopores also increased with increasing ageing temperature. A summary of the measurements are listed in Table S2.

3.2.2. The effect of Fe excess on the pore morphology

The FE-SEM image of non-stoichiometric sample 24aFe1.1St27 obtained by ageing a gel with 10 mol% excess Fe at 24 °C is shown in Fig. 5a. The morphology is similar to that of the stoichiometric samples 24aFe1St27 and 60aFe1St27 (Fig. 4b and c). This sample presents high external surface area ($26 \text{ m}^2 \text{ g}^{-1}$) and high $V_{\text{mes+mac}}$ fraction (99.3%) for details see Table S2. The PSD profile presents a

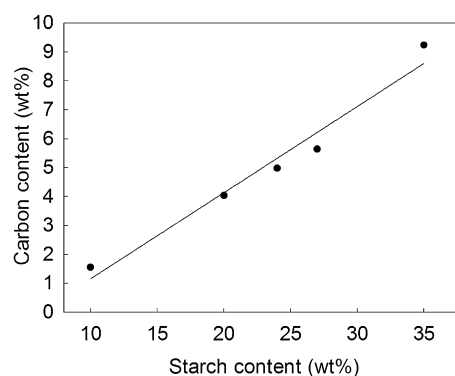


Fig. 2. The relationship between the residual carbon content of $\text{Li}_2\text{FeSiO}_4/\text{C}$ and starch content. The series 2 samples were prepared by ageing the gel at 60 °C. The solid circles are experimental data. The solid line is a linear fitting.

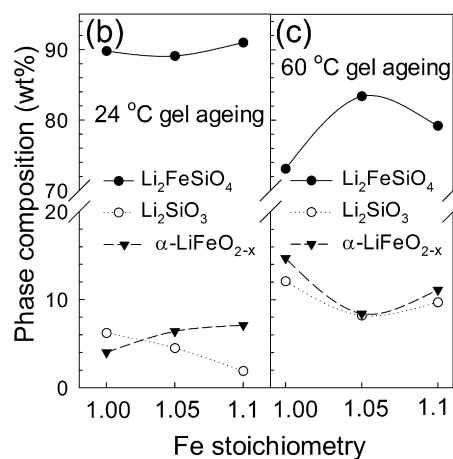
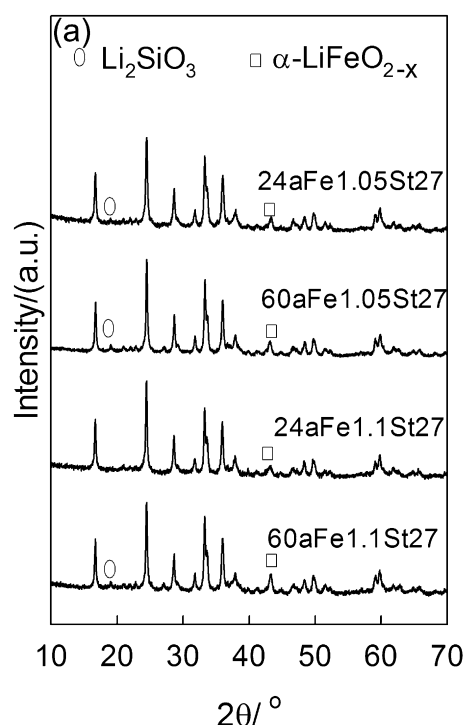


Fig. 3. (a) XRD patterns of the $\text{Li}_2\text{Fe}_x\text{SiO}_4/\text{C}$ ($x = 1.05, 1.1$) series 3 samples obtained by ageing the gel at 24 °C and 60 °C, using 27 wt% starch. (b) The relationship between the phase purity and Fe stoichiometry for different gel formation methods.

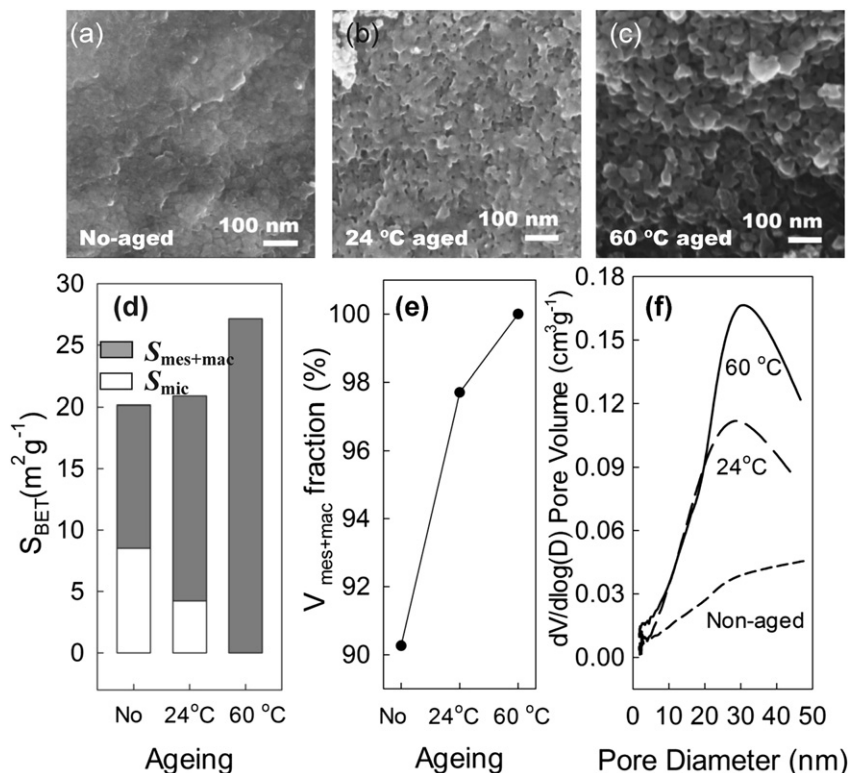


Fig. 4. FE-SEM images of the three $\text{Li}_2\text{FeSiO}_4/\text{C}$ series 1 samples (a) non-aged sample NoaFe1St27, (b) 24 °C aged sample 24aFe1St27, (c) 60 °C aged sample 60aFe1St27. The comparison of (d) microporous surface area (S_{mic}) and external surface area ($S_{\text{mes+mac}}$) (e) the fractions of mesopore and macropore volumes ($V_{\text{mes+mac}}$) of the total pore volume (V_{total}) and (f) pore size distributions (PSD) for the series 1 samples.

sharp peak at pore sizes around 30 nm, as shown in Fig. 5b. The TEM investigations further revealed that sample 24aFe1.1St27 consists of nanoparticles with nearly spherical shape (Fig. 6a). Fig. 6b shows a magnified image of the particle that is marked by a rectangle in Fig. 6a, clearly indicating that this particle is composed of nanoparticles with size of around ~20 nm. These particles are homogeneously covered by a ~2 nm thick amorphous or disordered carbon layer. Fig. 6c shows a high resolution TEM (HRTEM) image of a nanoparticle as marked by a rectangle in Fig. 6b. The measured lattice spacing in the HRTEM image is 0.21 nm and corresponds to the d-spacing of the {2 0 0} crystal planes of the α - LiFeO_{2-x} related phase, which was also observed in the XRD pattern. In order to further confirm the chemical compositions of these carbon-coated nanoparticles, elemental composition analysis

was performed by EDS. Fig. 6d shows the EDS spectra acquired from four different areas marked by circles in Fig. 6b. In circle 1, only Fe and C were found, which indicates that traces of iron metal formed during the carbothermal reduction are present. However, the small amount of Fe cannot be detected by XRD. In circle 2, Fe, Si, O, and C were observed, and the calculated chemical composition corresponds to the $\text{Li}_2\text{FeSiO}_4$ phase. In circle 3, the EDS spectrum shows a high C peak, which indicates that carbon as a main phase appears on the surface of the particle. In circle 4, only Fe, O, and C could be detected, meaning the particle is the α - LiFeO_{2-x} related phase as shown in Fig. 6c, as the lithium element cannot be detected by the EDS setup.

3.3. Electrochemical characterization

The initial specific charge/discharge capacity at a current density of C/16 ($C = 160 \text{ mA g}^{-1}$) for the $\text{Li}_2\text{FeSiO}_4/\text{C}$ composite prepared with different PVA-assisted sol–gel processes, different Fe stoichiometry, and 27 wt% starch are presented in Fig. 7a. The samples prepared by ageing at 24 °C with Fe stoichiometry of 1.0, 1.05, and 1.10 gave discharge capacities of 70, 110, and 163 mAh g^{-1} , respectively, during the first cycle, while the sample prepared without ageing and Fe stoichiometry of 1.0 showed a discharge capacity of only 27 mAh g^{-1} . This clearly shows a significant increase in the capacity with increasing Fe content and ageing of the gel. Fig. 7b shows that the samples prepared by ageing the gel at 60 °C with Fe contents of 1.0, 1.05, and 1.10 gave discharge capacities of 102, 115, and 123 mAh g^{-1} , respectively, during the first cycle. Here, the change in capacity with increasing Fe excess was rather small.

The rate capability of 24aFe1.1St27 prepared by ageing at 24 °C, with 10 mol% Fe excess, and 27 wt% starch is shown in Fig. 7c. For

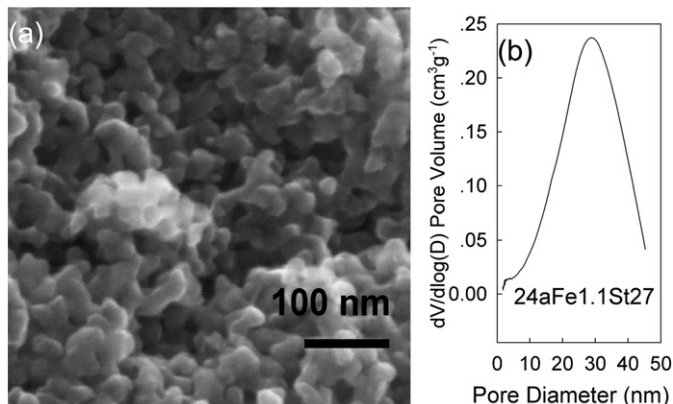


Fig. 5. (a) FE-SEM image and (b) PSD profile of sample 24aFe1.1St27.

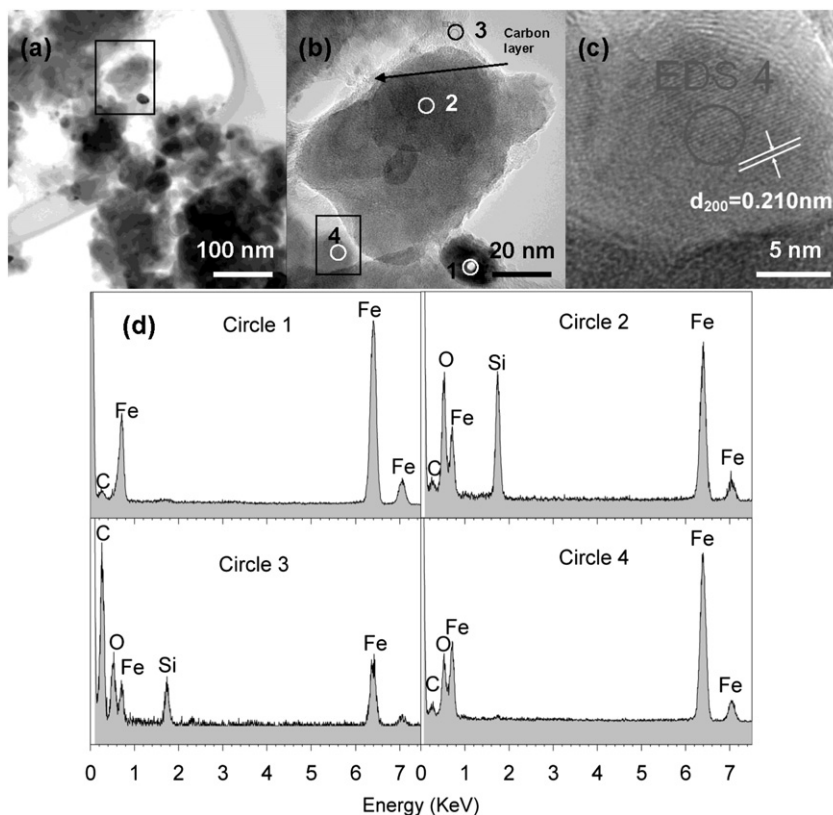


Fig. 6. (a–c) TEM images of sample 24aFe1.1St27, (d) EDS spectra taken from four different areas as marked by circles in (b).

the slowest rates (C/16), the discharge capacity gives a value of 165 mAh g^{-1} in the second charge/discharge cycle. The $\text{Li}_2\text{Fe}_{1.1}\text{SiO}_4/\text{C}$ composite cathode can deliver a discharge capacity of 130 mAh g^{-1} at a discharge rate of C/2 and a discharge capacity of

$\sim 110 \text{ mAh g}^{-1}$ at a discharge rate of 1 C. Fig. 7d gives the cycling stability of 24aFe1.1St27 at 1 C. The charge/discharge capacity decreased from 110 mAh g^{-1} and down to just over 100 mAh g^{-1} on the first 15 cycles, but increased slightly and stabilized after about

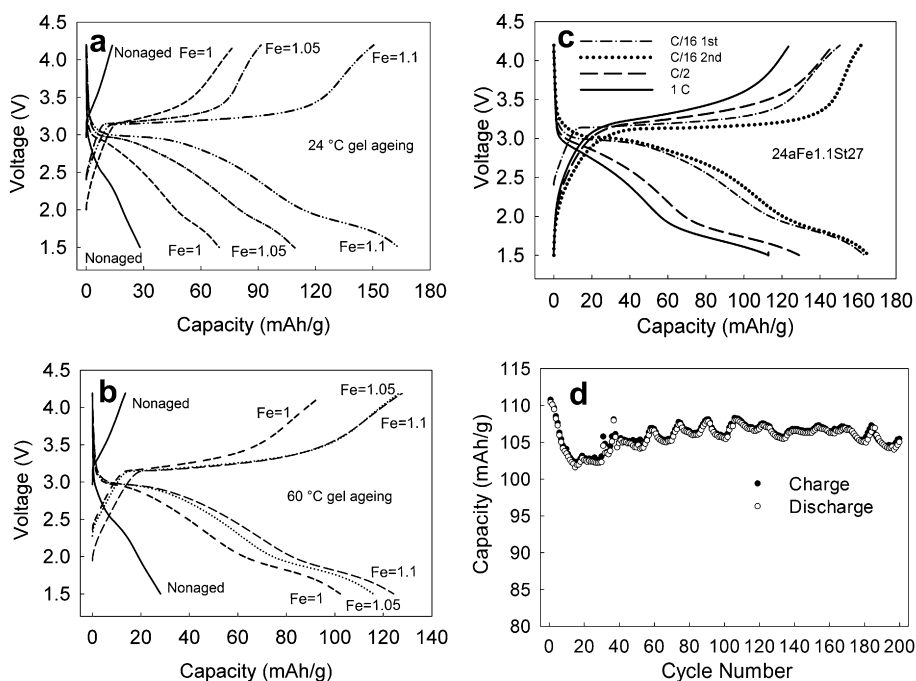


Fig. 7. Initial specific charge/discharge capacity for the $\text{Li}_2\text{FeSiO}_4/\text{C}$ samples prepared by no ageing, (a) ageing at 24°C , and (b) ageing at 60°C with different Fe stoichiometry at a current density of C/16 ($C = 160 \text{ mA g}^{-1}$). (c) Rate capability and (d) cycling stability of sample 24aFe1.1St27 prepared by ageing at 24°C , with 10 mol% Fe excess, and 27 wt% starch at a current density of 1 C.

the 16th cycle and maintained a value of around 106 mAh g^{-1} for the following 185 cycles, which is $\sim 96\%$ of the initial discharge capacity. The Coulombic efficiency is nearly 1, as shown in Fig. 7d.

4. Discussion

The electrochemical performance of the Li-ion battery is highly dependant on the morphology of the $\text{Li}_2\text{FeSiO}_4/\text{C}$ cathode material, which is determined by the gel formation process. It is also evident that the type and amount of secondary phases have a significant effect on the charge/discharge capacity. In the following sections the presented results will be discussed.

4.1. Effect of gel formation

Three different gel formation processes have been investigated here; no ageing, ageing for 10 h at 24°C , and ageing for 10 h at 60°C . Of these three methods the powders made without ageing the gel by far produced the lowest charge/discharged capacity. In order to understand this it is important to take a look at the gel formation and ageing mechanisms.

At the initial stage of the sol–gel process, which will be similar regardless of the ageing procedure, the hydrolysis and condensation of TEOS [33] occurred in the Li–Fe–Si transparent solution. In our case, where $\text{pH} < 2$ and the $\text{H}_2\text{O}/\text{Si}$ (w) ratio is much higher than 4, hydrolysis is expected to be completed at an early stage of the reaction, prior to any significant condensation [36]. Condensation between completely hydrolyzed species occurred by reaction-limited cluster–cluster aggregation, leading to weakly branched structures [37]. After adding the PVA solution, the presence of hydroxyl groups ($-\text{OH}$) in the repeating units of the PVA polymer were expected to produce strong interactions (hydrogen or covalent bonds) with the silanol groups of the silicate clusters [38]. In addition, the hydroxyl groups of PVA can chelate Fe^{3+} and Li^+ , forming complexes [39].

A schematic diagram for the proposed mechanisms explaining the three different gel formation procedures is proposed in Fig. 8. At the gelation point, the PVA-silicate spanning chains extend throughout the sol and weakly cross-link, causing an abrupt rise in the viscosity.

In the first method, the gel was kept non-covered and dried directly at 130°C , the liquid evaporated and the gel shrank rapidly. The shrinkage resulted from condensation between hydroxyl

groups ($-\text{OH}$) on the surface of the solid network. The spanning chains highly compacted together and formed high density and very fine pores. During the calcination and carbothermal reduction, this weak and finely porous structure collapsed, resulting in micropores being present in the product.

In the second method, the gel was covered and aged for 10 h at 24°C after the gelation point. Since the gel is allowed to age, the condensation reactions continue, and the small chains continue to diffuse and attach to the main network. Due to solubility differences, the attached material will deposit at the necks in between the particles and the network becomes stiffer and stronger. This gel was then dried at 130°C , which allowed the liquid to evaporate rapidly. The strengthened network can better withstand the capillary force and shrank less than the non-aged sample. After the calcination and carbothermal reduction, mesopores and micropores were present in the product.

In the third method, the gel was aged at higher temperature (60°C). The coarsening effect was reinforced and the skeleton of the gel was more effectively strengthened [40]. Small amounts of liquid phase formed due to syneresis and separated from the solid phase after the gel was aged at 60°C . In the same process composition segregation occurred, which lead to precipitation of LiNO_3 . During drying, the strongest porous structure was able to better withstand the capillary forces to reduce collapsing of the pores and the gel shrank less than the 24°C aged sample, giving a structure containing only meso- and macro-scale pores.

The micropores in the particles of the non-aged material are too small to obtain a suitable electrolyte complex arrangement. The calculated complex diameter for $\text{Li}(\text{EC})_2^+$ and $\text{Li}(\text{EC})_3^+$ using GULP code are 0.89 nm and 1.07 nm, respectively as shown in Fig. 9, which are comparable to the reported $\text{Li}(\text{propylene carbonate})_4^+$ diameter of 1.19 nm [18]. This means that the complexes are too large for the micropores ($\leq 2 \text{ nm}$) to achieve enough molecular mobility. Therefore, the samples that were not aged maintained a large amount of ineffective microporous surface area which shows poor electrochemical performance. When the 24°C or 60°C aged samples were applied in the Li-ion battery as cathode, the mesopores and macropores in the particles are large enough to allow penetration of more than two complexes of electrolyte into the cathode particles. Nearly all the surface area of the particles is effective for the electrochemical reaction, and hence the sample aged at 24°C or 60°C showed good electrochemical performance. Especially, the 60aFe1St27 sample shows a higher effective surface

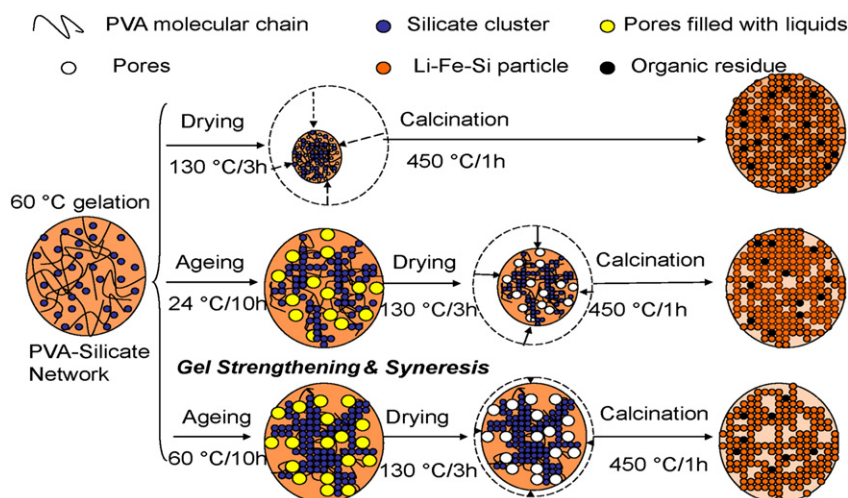


Fig. 8. Schematic diagram for the mechanism of the three different gel formation methods.

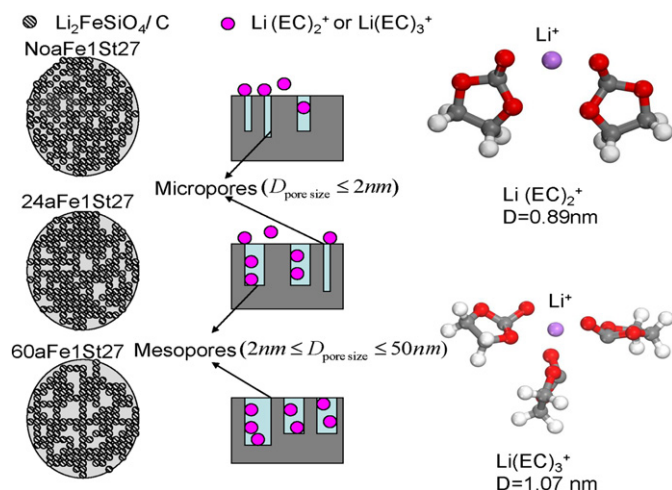


Fig. 9. Schematic diagram for the mechanism explaining the relationship between PSD and electrochemical performance.

area ($S_{mes+mac}$) than the 24aFe1St27 sample and possesses a large amount of electrochemically active material ($\text{Li}_2\text{FeSiO}_4$ and $\alpha\text{-LiFeO}_{2-x}$ related phase), thus 60aFe1St27 shows a higher capacity than 24aFe1St27 according to Fig. 7a and b. The mechanism to explain the relationship between the PSD and the electrochemical performance is shown in Fig. 9. In addition, the nanoporous structure also can sustain the changes of the phase and morphology evolution upon extended cycling [41]. Hence, the nanoporous $\text{Li}_2\text{FeSiO}_4/\text{C}$ cathode materials exhibited high cycling stability (Fig. 7d). Moreover, the capacity retention curve (Fig. 7d) shows the behaviour of a decreasing-increasing-stabilizing process (the “U” shape in the plot), which was also found in an amorphous $\text{MnO}_x\text{-C}$ anode material reported by Guo et al. [42]. This “U” shape evolution might associate with accumulation of defects/strain/stress energy in amorphous particles. In this work, the capacity retention curve showing the repeated “U” shape, might be due to activation of active materials in the inner particles [4] and gradual amorphization of the nanoporous $\text{Li}_2\text{FeSiO}_4/\text{C}$ cathode materials during extended cycling. Further work is needed to verify this.

The strengthened porous structure model obtained after ageing is in good agreement with the experimental results obtained from FE-SEM and nitrogen adsorption measurements (Figs. 4 and 5). In addition, some of the PVA chains trapped in the pores of the dry gels were difficult to pyrolyse and formed an organic residue after calcination at 450°C for 1 h. This was most significant for the non-aged gels. The PVA residue together with the starch formed the carbon coating on the surface of the oxide particles after the carbothermal reaction [43,44]. The effect of carbon content on the electrochemical performance is similar to our previous work [9]. The best battery performance was also achieved by using the nanoporous $\text{Li}_2\text{FeSiO}_4/\text{C}$ cathode materials with medium carbon content (5 wt%), i.e. 27% starch content.

4.2. Effect of Fe excess

For the series 3 samples prepared by ageing the gel at 24°C , the excess Fe seems to react with Li_2SiO_3 , giving high yield of $\text{Li}_2\text{FeSiO}_4$ and $\alpha\text{-LiFeO}_{2-x}$ related phase after the carbothermal reduction, as shown in the XRD patterns (Fig. 3). The content of electrochemically active material increased in the sample, reducing the amount of non-active material, i.e. Li_2SiO_3 phase. The combination of $\text{Li}_2\text{FeSiO}_4$ and $\alpha\text{-LiFeO}_{2-x}$ related phase seems to have a positive effect on the charge/discharge capacity (Fig. 7a), which can most

likely be attributed to the increased amount of the $\alpha\text{-LiFeO}_{2-x}$ related phase. In addition, traces of iron nanoparticles with high electronic conductivity might improve the charge transfer of the nanoporous $\text{Li}_2\text{FeSiO}_4/\text{C}$ composites during cycling. However, the capacity of the composites decreased for the samples with high content of metallic iron since the metallic iron itself is not electrochemically active, which was confirmed by our previous study [9].

For the series 3 samples prepared by ageing the gel at 60°C , a large amount of LiNO_3 precipitated from the gel giving an inhomogeneous gel. This results in a low yield of $\text{Li}_2\text{FeSiO}_4$ and high contents of Li_2SiO_3 and $\alpha\text{-LiFeO}_{2-x}$ related secondary phases, as shown in Fig. 3. The precipitation cannot be hindered by introducing excess amounts of Fe, the content of electrochemically active material did not increase obviously with Fe stoichiometry, and the battery performance will therefore only improve slightly by changing the Fe stoichiometry (Fig. 7b).

5. Conclusion

This paper reports on the effects of gel-formation parameters and Fe stoichiometry on the electrochemical properties of $\text{Li}_2\text{Fe}_x\text{SiO}_4/\text{C}$ ($x = 1.0, 1.05, 1.1$) nanocomposite. The pore size distribution greatly influenced the cycling behaviour, giving a discharge capacity close to theoretical (163 mAh g^{-1}) at low current densities. This was attributed to the large amount of meso- and macro-sized pores formed at higher ageing temperatures and longer ageing times. The PVA residue together with the starch formed the carbon coating on the surface of the oxide particles after the carbothermal reaction and improved the material conductivity and its rate capability. In addition, altering the Fe stoichiometry also imposed significant effects on the charge/discharge capacity. By increasing the Fe content the amount of undesirable impurities such as Li_2SiO_3 was greatly reduced, at the same time the amount of electrochemically active $\alpha\text{-LiFeO}_{2-x}$ related phase increased correspondingly, resulting in a material with improved cycling properties. The highest battery capacity obtained in this study resulted from a gel aged at 24°C for 10 h with Fe stoichiometry of 1.1 and medium carbon content.

Acknowledgements

The authors would like to thank Stein Hansen at Molab for help with analysis of carbon content of the samples. Per Erik Vullum (SINTEF) is acknowledged for help with the TEM images and EDS analysis. Hongye Chen (Department of Chemical Engineering, NTNU) is acknowledged for help with the GULP calculation.

Appendix A. Supplementary data

Supplementary data related to this article can be found at <http://dx.doi.org/10.1016/j.jpowsour.2013.02.023>.

References

- [1] B.L. Ellis, K.T. Lee, L.F. Nazar, *Chem. Mater.* 22 (2010) 691–714.
- [2] A. Nytén, A. Abouimrane, M. Armand, T. Gustafsson, J.O. Thomas, *Electrochem. Commun.* 7 (2005) 156–160.
- [3] R. Dominko, D.E. Conte, D. Hanzel, M. Gaberscek, J. Jamnik, J. Power Sources 178 (2008) 842–847.
- [4] X. Fan, Y. Li, J. Wang, L. Gou, P. Zhao, D. Li, L. Huang, S. Sun, *J. Alloys Compd.* 493 (2010) 77–80.
- [5] F. Vullum, D. Teeters, *J. Power Sources* 146 (2005) 804–808.
- [6] C. Deng, S. Zhang, B.L. Fu, S.Y. Yang, L. Ma, *Mater. Chem. Phys.* 120 (2010) 14–17.
- [7] M. Dahbi, S. Urbonaitė, T. Gustafsson, *J. Power Sources* 205 (2012) 456–462.
- [8] A. Nytén, M. Stjern Dahl, H. Rensmo, H. Siegbahn, M. Armand, T. Gustafsson, K. Edstrom, J.O. Thomas, *J. Mater. Chem.* 16 (2006) 3483–3488.

- [9] H. Zhou, M.-A. Einarsrud, F. Vullum-Bruer, *Solid State Ionics* 225 (2012) 585–589.
- [10] Z. Zheng, Y. Wang, A. Zhang, T. Zhang, F. Cheng, Z. Tao, J. Chen, *J. Power Sources* 198 (2012) 229–235.
- [11] Z. Yan, S. Cai, L. Miao, X. Zhou, Y. Zhao, *J. Alloys Compd.* 511 (2012) 101–106.
- [12] K.C. Kam, T. Gustafsson, J.O. Thomas, *Solid State Ionics* 192 (2011) 356–359.
- [13] C. Deng, S. Zhang, S.Y. Yang, B.L. Fu, L. Ma, *J. Power Sources* 196 (2011) 386–392.
- [14] L. Li, H. Guo, X. Li, Z. Wang, W. Peng, K. Xiang, X. Cao, *J. Power Sources* 189 (2009) 45–50.
- [15] M. Wu, T. Liao, Y. Wang, C. Wan, *J. Appl. Electrochem.* 34 (2004) 797–805.
- [16] T. Fukushima, Y. Matsuda, H. Hashimoto, R. Arakawa, *J. Power Sources* 110 (2002) 34–37.
- [17] D. Qu, H. Shi, *J. Power Sources* 74 (1998) 99–107.
- [18] M. Endo, T. Maeda, T. Takeda, Y.J. Kim, K. Koshiba, H. Hara, M.S. Dresselhaus, *J. Electrochem. Soc.* 148 (2001) A910–A914.
- [19] K. Nakanishi, N. Tanaka, *Acc. Chem. Res.* 40 (2007) 863–873.
- [20] M.-A. Einarsrud, M. Britt Kirkedelen, E. Nilsen, K. Mortensen, J. Samseth, *J. Non-Cryst. Solids* 231 (1998) 10–16.
- [21] P.J. Davis, C. Jeffrey Brinker, D.M. Smith, *J. Non-Cryst. Solids* 142 (1992) 189–196.
- [22] M.A. Einarsrud, E. Nilsen, A. Rigacci, G.M. Pajonk, S. Buathier, D. Valette, M. Durant, B. Chevalier, P. Nitz, F. Ehrburger-Dolle, *J. Non-Cryst. Solids* 285 (2001) 1–7.
- [23] J. Du, L.R. Corrales, *J. Phys. Chem. B* 110 (2006) 22346–22352.
- [24] X. Li, H. Guo, L. Li, X. Li, Z. Wang, H. Ou, K. Xiang, *Trans. Nonferrous. Met. Soc. China* 21 (2011) 529–534.
- [25] Y. Xu, Y. Li, S. Liu, H. Li, Y. Liu, *J. Power Sources* 220 (2012) 103–107.
- [26] L. Aldon, J.C. Jumas, *Solid State Sci.* 14 (2012) 354–361.
- [27] L. Chun, X. Wu, X. Lou, Y. Zhang, *Electrochim. Acta* 55 (2010) 3089–3092.
- [28] S. Ito, K. Nakaoka, M. Kawamura, K. Ui, K. Fujimoto, N. Koura, *J. Power Sources* 146 (2005) 319–322.
- [29] M.M. Rahman, J.-Z. Wang, M.F. Hassan, S. Chou, Z. Chen, H.K. Liu, *Energy Environ. Sci.* 4 (2011) 952–957.
- [30] M.N. Filippov, V.P. Gavrilenko, M.V. Kovalchuk, V.B. Mityukhlyayev, V.O. Yu, A.V. Rakov, V.V. Roddatis, P.A. Todua, A.L. Vasiliev, *Meas. Sci. Technol.* 22 (2011) 094014.
- [31] J.D. Gale, *J. Chem. Soc. Faraday Trans.* 93 (1997) 629–637.
- [32] A.K. Rappe, C.J. Casewit, K.S. Colwell, W.A. Goddard, W.M. Skiff, *J. Am. Chem. Soc.* 114 (1992) 10024–10035.
- [33] G. Mali, C. Sirisopanaporn, C. Masquelier, D. Hanzel, R. Dominko, *Chem. Mater.* 23 (2011) 2735–2744.
- [34] Y.T. Lee, C.S. Yoon, Y.S. Lee, Y.-K. Sun, *J. Power Sources* 134 (2004) 88–94.
- [35] R. Shannon, *Acta Crystallogr. Sect. A Found. Crystallogr.* 32 (1976) 751–767.
- [36] R.K. Iler, *The Chemistry of Silica*, Wiley, New York, 1979.
- [37] T. Witten Jr., L.M. Sander, *Phys. Rev. Lett.* 47 (1981) 1400–1403.
- [38] R. Bryaskova, D. Pencheva, G.M. Kale, U. Lad, T. Kantardjiev, *J. Colloid Interface Sci.* 349 (2010) 77–85.
- [39] Y. Ohtsuka, T. Watanabe, Y. Nishiyama, M. Matsuda, H. Yokoi, *J. Mater. Sci.* 29 (1994) 877–882.
- [40] S. Hæreid, M.-A. Einarsrud, G.W. Scherer, *J. Sol–Gel Sci. Technol.* 3 (1994) 199–204.
- [41] K.M. Shaju, P.G. Bruce, *Chem. Mater.* 20 (2008) 5557–5562.
- [42] J. Guo, Q. Liu, C. Wang, M.R. Zachariah, *Adv. Funct. Mater.* 22 (2012) 803–811.
- [43] S.W. Oh, S.T. Myung, S.M. Oh, K.H. Oh, K. Amine, B. Scrosati, Y.K. Sun, *Adv. Mater.* 22 (2010) 4842–4845.
- [44] T. Jiang, W. Pan, J. Wang, X. Bie, F. Du, Y. Wei, C. Wang, G. Chen, *Electrochim. Acta* 55 (2010) 3864–3869.